



# Epitaxial growth of NiCo<sub>2</sub>S<sub>4</sub>/Co<sub>9</sub>S<sub>8</sub>@Graphene heterogenous nanocomposites with high-rate lithium storage performance

Yun Song, Yu Meng, Pei Wang, Le Jiang, Zeyi Wu, Yingchang Jiang, Linfeng Hu\*

Department of Materials Science, Fudan University, Shanghai 200433, China



## ARTICLE INFO

### Article history:

Received 6 November 2017

Received in revised form

12 February 2018

Accepted 27 February 2018

Available online 1 March 2018

### Keywords:

Lithium storage

NiCo<sub>2</sub>S<sub>4</sub>/Co<sub>9</sub>S<sub>8</sub>

Epitaxial growth

Pseudo-capacitance

High-rate capability

## ABSTRACT

Constructing heterogeneous nanocomposite has attracted much attention for energy storage devices due to the fact that heterogeneous structure can boost charge transfer owing to the built-in-charge transfer driving force. Herein, a unique architecture for hetero-NiCo<sub>2</sub>S<sub>4</sub>/Co<sub>9</sub>S<sub>8</sub> nanocomposite anchored on Graphene (NiCo<sub>2</sub>S<sub>4</sub>/Co<sub>9</sub>S<sub>8</sub>@G) has been prepared by an epitaxial mechanism. The as-synthesized NiCo<sub>2</sub>S<sub>4</sub>/Co<sub>9</sub>S<sub>8</sub>@G electrode exhibits 662 and 490 mAh g<sup>-1</sup> capacity at the first discharge/charge cycle and can be maintained at 323 mAh g<sup>-1</sup> after 4000 cycles (from 2nd cycle only 0.008% decay per cycle) at an ultrahigh current density of 10 A g<sup>-1</sup>. Moreover, NiCo<sub>2</sub>S<sub>4</sub>/Co<sub>9</sub>S<sub>8</sub>@G electrode can be full charged within 11 s while still achieving a specific capacity of 133 mAh g<sup>-1</sup> at a current density of 40 A g<sup>-1</sup>. This fascinating high-rate capability is attributed to the pseudo-capacitance contribution which can be further verified by kinetics model. This pseudo-capacitance originating from hetero structure sheds new light on the development of high-rate performance anode materials.

© 2018 Elsevier B.V. All rights reserved.

## 1. Introduction

Lithium ion batteries (LIBs) have been reported to be one of the most promising energy storage devices for their high energy density, suitable working temperature, high voltage and environmental friendliness [1–5]. However, LIBs has been challenging to extend this success to power electric vehicles (EVs) due to the lack of high-performance anode materials. Although considerable research has been made to exploring new anode materials with high specific capacity and good cycling stability, [6–8] few attention has been paid to the high-rate performance which plays an important part in EVs [9]. Therefore, the rational design and facile synthesis of new anode materials with high-rate performance and long cycling lifespan is rather desired.

To obtain high-rate performance anode materials, the critical step lies in choosing appropriate host materials with optimized structures. The host materials are expected to meet following requirements: high theoretical lithium storage capacities, long cycling stability and high intrinsic conductivity [10,11]. Among various anode materials, NiCo<sub>2</sub>S<sub>4</sub> has been investigated due to its high theoretical capacity and high conductivity [12–16]. Xia et al.

have reported that NiCo<sub>2</sub>S<sub>4</sub> exhibits intrinsically metallic or conductive behavior [13]. Additionally, our previous work has demonstrated high-rate performance for LIB anodes in two-dimensional (2D) NiCo<sub>2</sub>S<sub>4</sub> hexagonal nanosheets with a specific capacity of 607 mAh g<sup>-1</sup> after 800 cycles at a current density of 2 A g<sup>-1</sup> [17]. However, up to date, few NiCo<sub>2</sub>S<sub>4</sub>-based anodes could endure long cycles (>1000 cycles) due to the lack of structure stability upon lithiation/delithiation process, which seriously impedes the application of NiCo<sub>2</sub>S<sub>4</sub>.

In recent years, cobalt sulfide, Co<sub>9</sub>S<sub>8</sub>, as another emerging alternative electrode for high-performance LIBs, has exhibited remarkable electrochemical properties. Compared to NiCo<sub>2</sub>S<sub>4</sub>, Co<sub>9</sub>S<sub>8</sub> exhibits robust cycle retention and chemical stability owing to its high electroactivity and good electronic conductivity, thus ensuring stable reversible capacity [18–23]. Combining the advantage of high conductivity of NiCo<sub>2</sub>S<sub>4</sub> and high structural stability of Co<sub>9</sub>S<sub>8</sub>, it is rational that the NiCo<sub>2</sub>S<sub>4</sub>/Co<sub>9</sub>S<sub>8</sub> composite should be highly desirable for high-performance lithium ion storage. More importantly, it has been reported that heterostructures coupling well-dispersed nanograins generally show superior pseudocapacitive effect due to ultrafast charge transfer and electron mobility in the hetero-structure interface [24–26]. Since pseudocapacitive effect generally leads to high-rate capability and long-life span in power LIBs [9,27–29], NiCo<sub>2</sub>S<sub>4</sub>/Co<sub>9</sub>S<sub>8</sub> hetero-structure in a nanoscale should be very promising to improve the

\* Corresponding author.

E-mail address: [linfenghu@fudan.edu.cn](mailto:linfenghu@fudan.edu.cn) (L. Hu).

rate capability and stability. However, there are still no reports on the rational design of NiCo<sub>2</sub>S<sub>4</sub>/Co<sub>9</sub>S<sub>8</sub> nanocomposite as anode materials for lithium ion storage.

Motivated by this consideration, in the present work, we design a unique architecture for NiCo<sub>2</sub>S<sub>4</sub>/Co<sub>9</sub>S<sub>8</sub> heterostructured nanocrystals anchored on Graphene (NiCo<sub>2</sub>S<sub>4</sub>/Co<sub>9</sub>S<sub>8</sub>@G) by an epitaxial growth mechanism. The as-synthesized NiCo<sub>2</sub>S<sub>4</sub>/Co<sub>9</sub>S<sub>8</sub>@G anode exhibited 662 and 490 mAh g<sup>-1</sup> capacity at the first discharge/charge cycle and also can be maintained at 323 mAh g<sup>-1</sup> after 4000 cycles (from 2nd cycle only 0.008% decay per cycle) at an ultrahigh current density of 10 A g<sup>-1</sup>. Such a high-rate capacity and stability is much superior to previously reported NiCo<sub>2</sub>S<sub>4</sub> or Co<sub>9</sub>S<sub>8</sub> systems. Further kinetics model has revealed that the expected pseudo capacitance in NiCo<sub>2</sub>S<sub>4</sub>/Co<sub>9</sub>S<sub>8</sub>@G composites plays an important role in excellent high rate performance. This pseudo capacitance originating from hetero-stacking structure sheds new light on the development of high-rate performance anode materials.

## 2. Experimental section

### 2.1. Synthesis of samples

Graphene (sheet size: 0.5–2 μm, thickness: 0.8 nm, monolayer rate: 80%) was purchased from Nanjing XFANO Materials Tech Co., Ltd, cobalt chloride (CoCl<sub>2</sub>·6H<sub>2</sub>O), nickel chloride (NiCl<sub>2</sub>·6H<sub>2</sub>O) and hexamethylenetetramine (HMT) were purchased from Sino-pharm Chemical Reagent Co., Ltd and directly used without further purification. NiCo<sub>2</sub>S<sub>4</sub>/Co<sub>9</sub>S<sub>8</sub>@G nanocomposite was synthesized by a two-step strategy consisting of homogeneous precipitation and further thermal annealing. First, 5 mmol of cobalt chloride (CoCl<sub>2</sub>·6H<sub>2</sub>O), 2.5 mmol of nickel chloride (NiCl<sub>2</sub>·6H<sub>2</sub>O) and 45 mmol of hexamethylenetetramine (HMT) were dissolved in 1000 cm<sup>3</sup> of deionized water. This solution was refluxed for 6 h under continuous magnetic stirring and nitrogen protection. The light-pink precipitate was recovered by filtration, washed with deionized water and anhydrous ethanol in turn, and finally air-dried at room temperature. Based on previous report, this pink precipitate is Ni<sub>1/3</sub>Co<sub>2/3</sub>(OH)<sub>2</sub> (NiCo-hydroxide) [17]. The light-pink precipitate was obtained by the thermal annealing at 500 °C for 2 h with a heating rate of 1 °C min<sup>-1</sup>, and the product was ball-milled with Graphene in a weight ratio of 80:20 for 6 h under Ar atmosphere by using a planetary mill at 300 rpm with a 30:1 ball-to-powder ratio. Finally, the post milled sample was subjected to thermal annealing at 400 °C for 6 h under H<sub>2</sub>S gas, and NiCo<sub>2</sub>S<sub>4</sub>/Co<sub>9</sub>S<sub>8</sub>@G was obtained.

### 2.2. Characterizations

To identify the phase purity and crystal structures of the products, X-ray diffraction (XRD) measurements were carried out on a Bruker D8 ADVANCE X-ray diffractometer with Cu Kα radiation (λ = 1.5406 Å). The XRD profiles were analyzed with the Rietveld refinement program RIETAN-2000. The FTIR spectrum was recorded on Nicolet iS50 FT-IR spectrometer. The morphology and microstructure of the products were examined by the field-emission scanning electron microscope (FESEM, JEOL JSM-7600F) and transmission electron microscope (TEM, FEI Tecnai G2 F 20 S-Twin).

### 2.3. Electrode fabrication and electrochemical measurements

To fabricate working electrodes, active powder, conductive carbon (Super P) and binder (polyvinylidene fluoride, PVDF) were mixed in a weight ratio of 70:15:15; 1-methyl-2-pyrrolidinone

solvent (Aldrich, 99%) was added to form slurry. The well-mixed slurry was coated onto a Cu foil as a current collector using a doctor blade technique and then dried under vacuum at 80 °C for 12 h. Coin-type half-cells were assembled inside an argon-filled glove box (<5 ppm, H<sub>2</sub>O and O<sub>2</sub>), using Li metal foils as counter electrodes, porous polypropylene membrane as separators, and 1.0 M LiPF<sub>6</sub> in a mixture of ethylene carbonate and dimethyl carbonate (1:1) as electrolyte. The charge-discharge cycling was performed within the voltage range of 0.01–3.0 V vs. Li/Li<sup>+</sup> on a battery test instrument (CT2001A, LAND) under constant temperature of 25 °C. Cyclic voltammetry (CV) was performed on the electrochemical workstation (CHI660e). All the electrochemical tests were carried out at room temperature. All the current densities and specific capacities presented in this paper are calculated based on the total mass of the composite.

## 3. Results and discussion

### 3.1. Characterization of NiCo<sub>2</sub>S<sub>4</sub>/Co<sub>9</sub>S<sub>8</sub>@G composites

The phase structure of the composite is determined by Rietveld refinement of the X-ray diffraction (XRD) data in the 2θ region between 10 and 80°. The Rietveld refinement pattern of the composite is shown in Fig. 1a. The final refinement is carried out with a two-phase model containing NiCo<sub>2</sub>S<sub>4</sub> and Co<sub>9</sub>S<sub>8</sub>. The calculated pattern shows good agreement with the observed pattern. The mass ratio of the NiCo<sub>2</sub>S<sub>4</sub> and Co<sub>9</sub>S<sub>8</sub> phases is 58: 42. The goodness-of-fit parameter S is 1.03. The XRD pattern of Co<sub>9</sub>S<sub>8</sub> can be indexed to the standard JCPDS No. 02-1459, while the NiCo<sub>2</sub>S<sub>4</sub> can be indexed to the standard JCPDS No. 20-0782. The Graphene phase was not detected in XRD analysis due to its ultrathin nature and amorphous state. We employ FTIR spectroscopy to investigate the existence of Graphene and chemical interaction between NiCo<sub>2</sub>S<sub>4</sub>/Co<sub>9</sub>S<sub>8</sub> sheet and Graphene, as shown in Fig. 1b. As for ball-milled Graphene, the bands at 1110 and 1570 cm<sup>-1</sup> are related to the skeletal vibration of C-O and C-C. Moreover, the peak at ~2300 cm<sup>-1</sup> can be indexed to the spectrum of CO<sub>2</sub> [30,31]. The presence of CO<sub>2</sub> is due to the fact that oxygen in air is adsorbed and reacts with the as-prepared sample exposed to air. In addition, the broad absorption band at 3300 and 3600 cm<sup>-1</sup> derives from the presence of free hydroxyl groups, which is attributed to the water in the KBr during sample preparation [30]. These C-O, C-C and -OH footprints of ball-milled Graphene sample are observed in NiCo<sub>2</sub>S<sub>4</sub>/Co<sub>9</sub>S<sub>8</sub>@G composite, indicating the existence of Graphene. Importantly, one new characteristic peak at 625 cm<sup>-1</sup> is identified for the NiCo<sub>2</sub>S<sub>4</sub>/Co<sub>9</sub>S<sub>8</sub>@G composite. As compared with literature, this peak clearly corresponds to the C-S stretches, providing a proof of the electronic interaction between NiCo<sub>2</sub>S<sub>4</sub>/Co<sub>9</sub>S<sub>8</sub> and Graphene [30,32]. The formation of C-S bonds is due to the S atoms from the NiCo<sub>2</sub>S<sub>4</sub>/Co<sub>9</sub>S<sub>8</sub> or H<sub>2</sub>S interact with the unbounded C atoms at the edge of the defective Graphene upon ball milling and further solid-gas reaction. It has been reported that the C-S bond can successfully support and stabilize the layered structure [30,31]. Fig. 1c and d shows the X-ray absorption spectra (XAS) at Co and Ni K-edge for NiCo<sub>2</sub>S<sub>4</sub>/Co<sub>9</sub>S<sub>8</sub>@G composite. Compared with the reference spectra of corresponding metal oxides, the valence state of Ni in NiCo<sub>2</sub>S<sub>4</sub>/Co<sub>9</sub>S<sub>8</sub>@G composite is around 2<sup>+</sup>, and that of Co is a little lower than 2<sup>+</sup>. Such a result further confirms the presence of Co<sub>9</sub>S<sub>8</sub> phase in the product.

Transmission electronic microscope (TEM) image of the product in Fig. 2a and b shows large amounts of particle-like objects and Graphene matrix, indicating NiCo<sub>2</sub>S<sub>4</sub>/Co<sub>9</sub>S<sub>8</sub> composites are dispersed uniformly on the surface of Graphene. The mean lateral size of NiCo<sub>2</sub>S<sub>4</sub>/Co<sub>9</sub>S<sub>8</sub> nanocrystal ranges from 50 to 100 nm. A

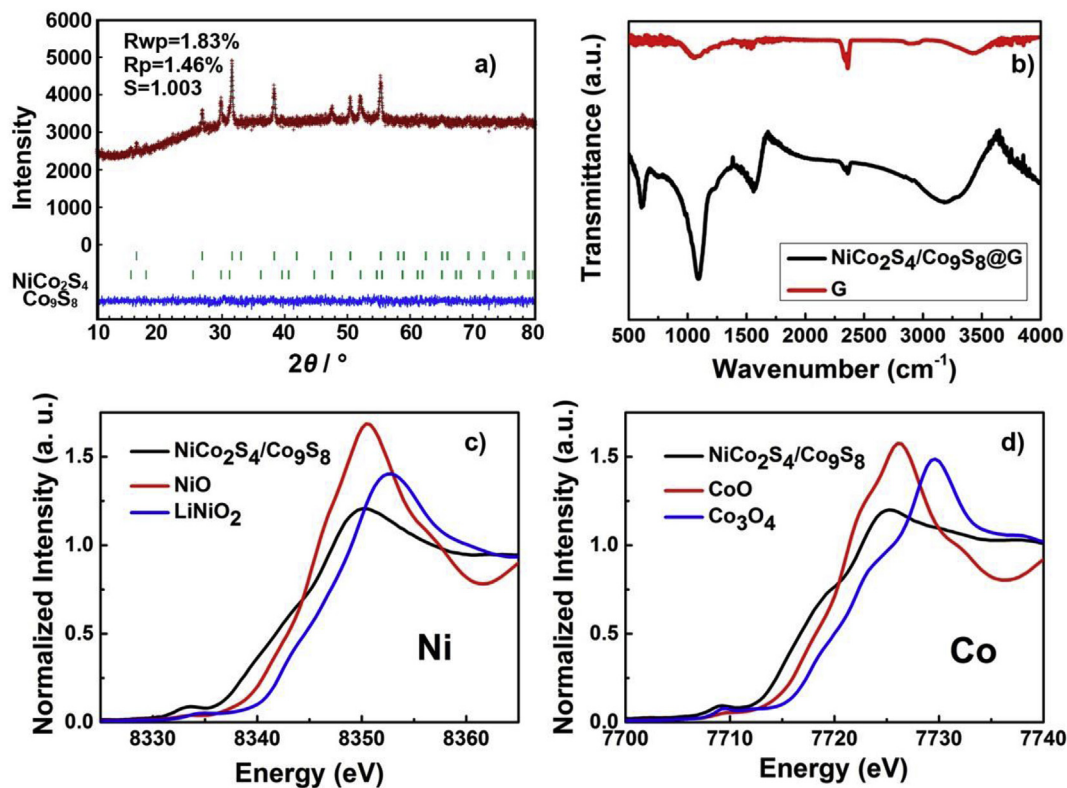


**Fig. 1.** (a) Rietveld refinement of XRD data for NiCo<sub>2</sub>S<sub>4</sub>/Co<sub>9</sub>S<sub>8</sub>@G composite. (b) FTIR spectra of NiCo<sub>2</sub>S<sub>4</sub>/Co<sub>9</sub>S<sub>8</sub>@G composite and Graphene. The X-ray absorption spectra (XAS) at (c) Co and (d) Ni K-edge for NiCo<sub>2</sub>S<sub>4</sub>/Co<sub>9</sub>S<sub>8</sub>@G composite.

high-resolution TEM (HRTEM) is carried out to detect the microstructure of NiCo<sub>2</sub>S<sub>4</sub>/Co<sub>9</sub>S<sub>8</sub>@G composite, as shown in Fig. 2c. The image clearly shows the interface between NiCo<sub>2</sub>S<sub>4</sub> and Co<sub>9</sub>S<sub>8</sub> grains. The lattice-fringe spacing of the NiCo<sub>2</sub>S<sub>4</sub> grain is 2.81 Å, which corresponds to the *d* spacing of the (311) plane; while the (311) plane of the Co<sub>9</sub>S<sub>8</sub> grain shows a slightly larger spacing of 2.93 Å. Fig. 2d shows the corresponding SAED pattern of NiCo<sub>2</sub>S<sub>4</sub>/Co<sub>9</sub>S<sub>8</sub> nanocomposites, suggesting that strong spherical spots form Co<sub>9</sub>S<sub>8</sub> phase and weak diffraction spots from NiCo<sub>2</sub>S<sub>4</sub> phase are simultaneously present. Note that the crystallographic orientation of Co<sub>9</sub>S<sub>8</sub> (111) plane parallels to that of (111) plane of NiCo<sub>2</sub>S<sub>4</sub> in this SAED pattern. This result implies that the (111) plane of Co<sub>9</sub>S<sub>8</sub> might be epitaxially grown on the (111) plane of NiCo<sub>2</sub>S<sub>4</sub>. Structurally, both NiCo<sub>2</sub>S<sub>4</sub> and Co<sub>9</sub>S<sub>8</sub> crystals belong to cubic structure with *a* = 9.387 Å (S. G. *Fd*  $\bar{3}m$ ) and *a* = 9.927 Å (S. G. *Fd*  $\bar{3}m$ ), respectively (see Fig. 3a and b) [17,19]. To carefully analyzing both crystal structures, top-view structures of NiCo<sub>2</sub>S<sub>4</sub> (111) plane and Co<sub>9</sub>S<sub>8</sub> (111) plane are depicted in Fig. 3c and d, respectively. Interestingly, these two planes present close similarities in terms of hexagonal-arranged S atomic configuration. In NiCo<sub>2</sub>S<sub>4</sub> (111) plane, the Co–S, Ni–S bond distance is close to 2.265 Å, 2.180 Å, respectively. In Co<sub>9</sub>S<sub>8</sub> (111) plane, the Co–S bond displays a distance of 2.208 Å, respectively. Therefore, the in-plane lattice mismatch between Co–S bond in NiCo<sub>2</sub>S<sub>4</sub> (111) plane and Co<sub>9</sub>S<sub>8</sub> (111) plane can be estimated to be as small as  $(d_{\text{NiCo}_2\text{S}_4} - d_{\text{Co}_9\text{S}_8})/d_{\text{NiCo}_2\text{S}_4} = (2.265 - 2.208)/2.265 = 2.52\%$ . Analogously, the in-plane lattice mismatch between Ni–S bond in NiCo<sub>2</sub>S<sub>4</sub> (111) plane and Co–S bond in Co<sub>9</sub>S<sub>8</sub> (111) plane can be estimated to 1.28%. Both of these values are less than 5%. This high structural compatibility provides important evidence that Co<sub>9</sub>S<sub>8</sub> nanograin was planar epitaxially grown on the NiCo<sub>2</sub>S<sub>4</sub> (111) plane to form NiCo<sub>2</sub>S<sub>4</sub>/Co<sub>9</sub>S<sub>8</sub> hetero-structure in a nanoscale.

### 3.2. Electrochemical characteristics of NiCo<sub>2</sub>S<sub>4</sub>/Co<sub>9</sub>S<sub>8</sub>@G composites

The electrochemical properties of NiCo<sub>2</sub>S<sub>4</sub>/Co<sub>9</sub>S<sub>8</sub>@G composite sample were characterized in coin cells with Li foil as the counter electrode. Fig. 4a shows the cyclic voltammetry (CV) curves of the NiCo<sub>2</sub>S<sub>4</sub>/Co<sub>9</sub>S<sub>8</sub>@G composite, which are collected at a scan rate of 0.1 mV s<sup>-1</sup> in a potential window of 0.01–3.00 V versus Li<sup>+</sup>/Li. To distinguish the oxidation and reduction reactions induced by the NiCo<sub>2</sub>S<sub>4</sub>@G composite, the CV curves of NiCo<sub>2</sub>S<sub>4</sub>@G are studied under the same testing conditions, as shown in Fig. S1. For NiCo<sub>2</sub>S<sub>4</sub>@G composite, in the first cathodic scan, two intense peaks located at 1.29 V and 1.09 V are observed, which can be attributed to the Li<sup>+</sup> insertion into NiCo<sub>2</sub>S<sub>4</sub> to form Li<sub>*x*</sub>NiCo<sub>2</sub>S<sub>4</sub> and subsequent conversion reaction between Li<sup>+</sup> with NiCo<sub>2</sub>S<sub>4</sub>, respectively. A broad bump between 0.72 and 0.10 V is assigned to formation of SEI film and Li<sup>+</sup> insertion into Graphene layers [16]. For NiCo<sub>2</sub>S<sub>4</sub>/Co<sub>9</sub>S<sub>8</sub>@G composite, in the first discharge process, three cathodic peaks at 1.40 V, 1.25 V and 1.16 V are observed. The peak at 1.40 V and 1.25 V can be attributed to the reduction of Ni<sup>2+</sup> and Co<sup>3+</sup> of NiCo<sub>2</sub>S<sub>4</sub> into metallic Ni and Co. These two peaks shift to higher potential, as compared to 1.29 V and 1.09 V of the NiCo<sub>2</sub>S<sub>4</sub>@G composite. This may result from tuning effects of Co<sub>9</sub>S<sub>8</sub> to the redox reaction potential of NiCo<sub>2</sub>S<sub>4</sub>. The peak at 1.16 V is assigned to the reduction of Co<sub>9</sub>S<sub>8</sub>, which is slightly higher than other reported results (1.06 V [19] and 1.07 V [21]). These peak shifts of NiCo<sub>2</sub>S<sub>4</sub> and Co<sub>9</sub>S<sub>8</sub> give a strong proof of synergistic electrochemical effect between NiCo<sub>2</sub>S<sub>4</sub> and Co<sub>9</sub>S<sub>8</sub>. A similar broad bump is observed at 0.67 V, which is also slightly shifted to lower potential as compared with that of NiCo<sub>2</sub>S<sub>4</sub>@G composite. In the first charge process, two oxidation peaks located at 2.10 V and 2.42 V refer to the oxidation reactions back to NiCo<sub>2</sub>S<sub>4</sub> and Co<sub>9</sub>S<sub>8</sub> [16,19,21]. In the second cycle, cathodic peaks shift to 1.25 V, 1.70 V, and anodic peaks shift to

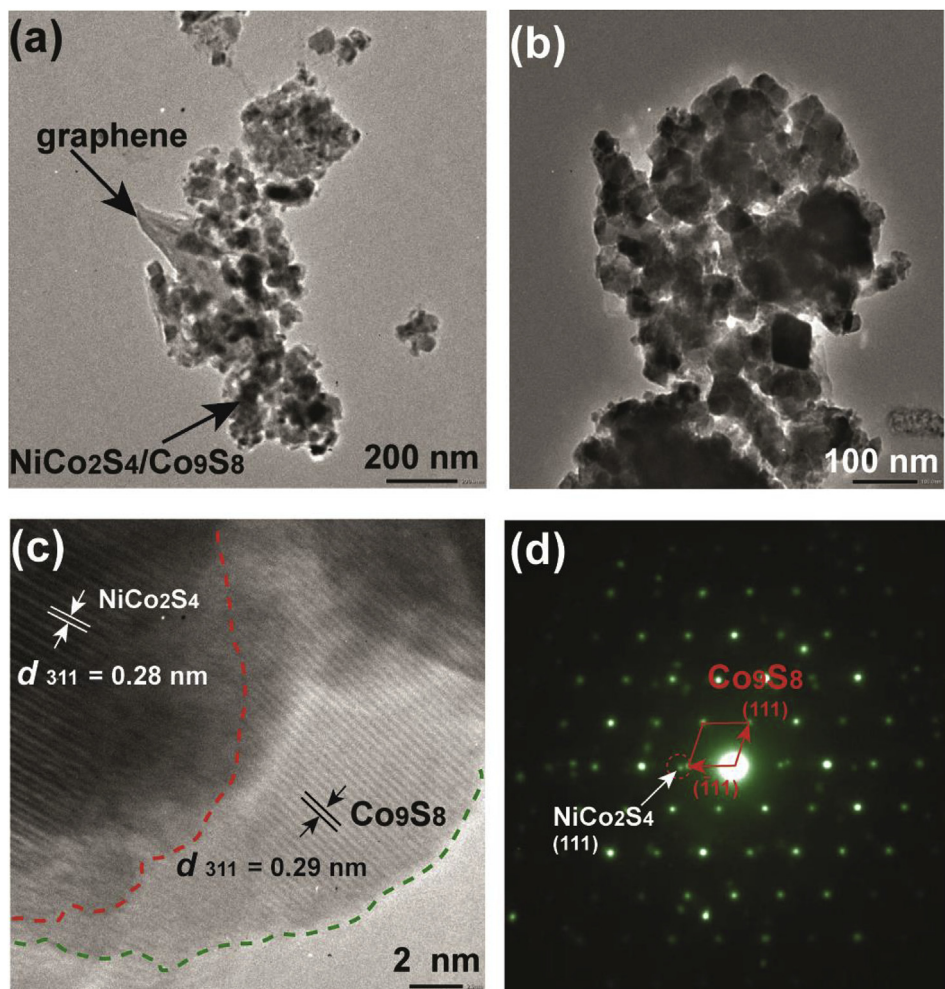


**Fig. 2.** (a) TEM and (b) enlarged TEM image of NiCo<sub>2</sub>S<sub>4</sub>/Co<sub>9</sub>S<sub>8</sub>@G composite; (c) HRTEM of NiCo<sub>2</sub>S<sub>4</sub>/Co<sub>9</sub>S<sub>8</sub>@G composite showing the interface between NiCo<sub>2</sub>S<sub>4</sub> and Co<sub>9</sub>S<sub>8</sub> domains. (d) The corresponding SAED pattern.

2.10 V, 2.42 V. This is due to the irreversible structural change of NiCo<sub>2</sub>S<sub>4</sub>/Co<sub>9</sub>S<sub>8</sub>@G nanocomposites after the first discharge [29]. It is noteworthy that the CV curves almost overlap from the 2<sup>nd</sup> to the 6<sup>th</sup> cycles, reflecting the excellent reversibility of the electrochemical reactions in NiCo<sub>2</sub>S<sub>4</sub>/Co<sub>9</sub>S<sub>8</sub>@G composite and ensuring prolonged cycling stability [9].

The long-term cycling performance of NiCo<sub>2</sub>S<sub>4</sub>/Co<sub>9</sub>S<sub>8</sub>@G electrode at a high current density of 10 A g<sup>-1</sup> is shown in Fig. 4b. In the initial cycle, NiCo<sub>2</sub>S<sub>4</sub>/Co<sub>9</sub>S<sub>8</sub>@G electrode delivers a discharge capacity of 662 mAh g<sup>-1</sup> and a charge capacity of 490 mAh g<sup>-1</sup>, with a low corresponding coulombic efficiency of 74.1%. The low coulombic efficiency in the first cycle is ascribed to the initial formation of SEI layers and the incomplete reduction of Li<sub>2</sub>S. From the third cycling onward, the coulombic efficiency quickly increases to above 95%. This rapid improvement of coulombic efficiency is originated from the optimized hetero structure, in which NiCo<sub>2</sub>S<sub>4</sub>/Co<sub>9</sub>S<sub>8</sub> nanocrystal contact with 2D Graphene matrix [29]. After 4000 cycles, the specific capacity of NiCo<sub>2</sub>S<sub>4</sub>/Co<sub>9</sub>S<sub>8</sub>@G electrode is stabilized at 323 mAh g<sup>-1</sup>, with a capacity decay less than 0.008% per cycle from the second cycle onward. Moreover, at this current density, the NiCo<sub>2</sub>S<sub>4</sub>/Co<sub>9</sub>S<sub>8</sub>@G electrode can be fully charged within 200 s. For comparison, the long-cycling performance of NiCo<sub>2</sub>S<sub>4</sub>@G is shown in Fig. S2. Apparently, the NiCo<sub>2</sub>S<sub>4</sub>/Co<sub>9</sub>S<sub>8</sub>@G exhibits much improved cycling stability as compared with the NiCo<sub>2</sub>S<sub>4</sub>@G, which stems from the superior structure stability of Co<sub>9</sub>S<sub>8</sub> as reported

previously [18–23]. On the other hand, the rate performance of Co<sub>9</sub>S<sub>8</sub>@G is shown in Fig. S3. It is obvious that NiCo<sub>2</sub>S<sub>4</sub>/Co<sub>9</sub>S<sub>8</sub>@G exhibits much improved rate performance and higher capacity as compared with the Co<sub>9</sub>S<sub>8</sub>@G. As expected, the NiCo<sub>2</sub>S<sub>4</sub>/Co<sub>9</sub>S<sub>8</sub>@G electrode show fascinating lithium ion storage performance, combining the advantage of high conductivity of NiCo<sub>2</sub>S<sub>4</sub> and high structural stability of Co<sub>9</sub>S<sub>8</sub>. Moreover, this ultra-long cycling performance at a high density (10 A g<sup>-1</sup>) of NiCo<sub>2</sub>S<sub>4</sub>/Co<sub>9</sub>S<sub>8</sub>@G nanocrystal is much superior to other reported NiCo<sub>2</sub>S<sub>4</sub> or Co<sub>9</sub>S<sub>8</sub> systems, as compared in Table 1.

The rate capability of NiCo<sub>2</sub>S<sub>4</sub>/Co<sub>9</sub>S<sub>8</sub>@G electrode in the range of 0.01–3.00 V is evaluated at various current densities (0.2–40 A g<sup>-1</sup>), as shown in Fig. 4c. The NiCo<sub>2</sub>S<sub>4</sub>/Co<sub>9</sub>S<sub>8</sub>@G exhibits much higher reversible capacity of 838, 737, 677, 654 and 578 mAh g<sup>-1</sup> at current densities of 0.2, 0.4, 0.8, 1 and 2 A g<sup>-1</sup>, respectively. In addition, when the current density is further increased to 5, 10, 15, 20, 25, 30, 35 and 40 A g<sup>-1</sup>, the NiCo<sub>2</sub>S<sub>4</sub>/Co<sub>9</sub>S<sub>8</sub>@G electrode shows excellent rate capability of 477, 325, 257, 199, 173, 141, 135 and 133 mAh g<sup>-1</sup>, which can be fully charged within 360, 120, 60, 36, 24, 17, 13, and 11 s, respectively.

It has been demonstrated that there are three charge storage mechanism in battery system: i) the diffusion-controlled faradic storage mechanism from conversion and alloying reaction, which take place in the bulk phase, with the ions deeply diffused into interlayer gaps; ii) pseudocapacitive charge storage mechanism

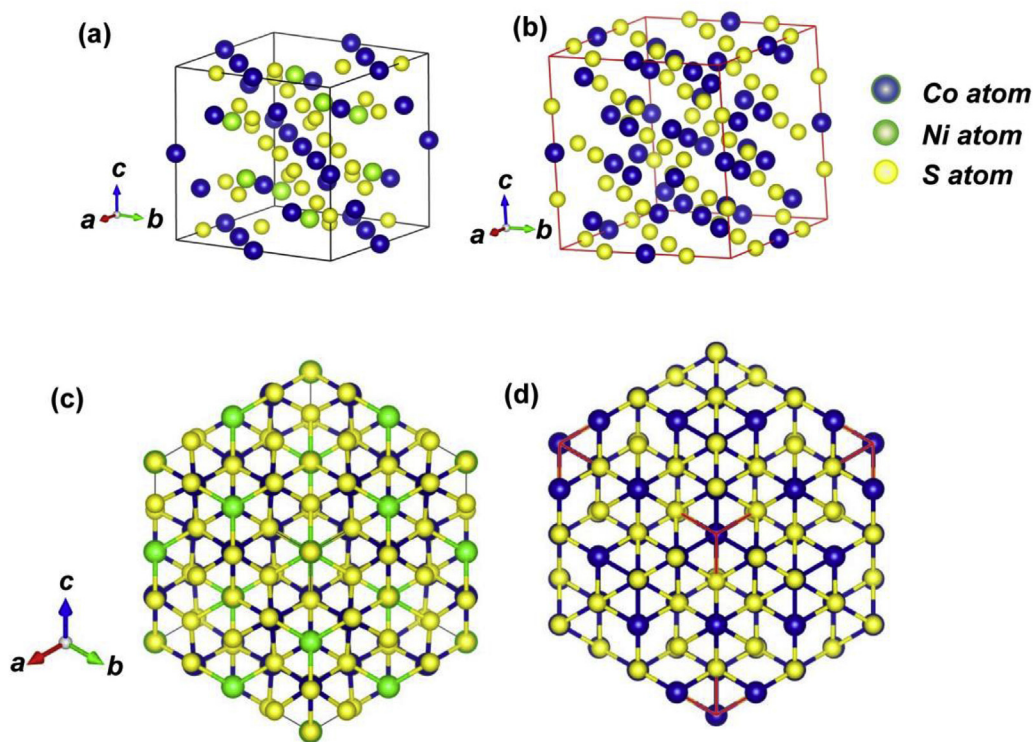


Fig. 3. Schematic illustration of (a) NiCo<sub>2</sub>S<sub>4</sub> and (b) Co<sub>9</sub>S<sub>8</sub> unit cell [17,19]. Top-view atomic structures of (c) Co<sub>9</sub>S<sub>8</sub> (111) plane and (d) NiCo<sub>2</sub>S<sub>4</sub> (111) plane.

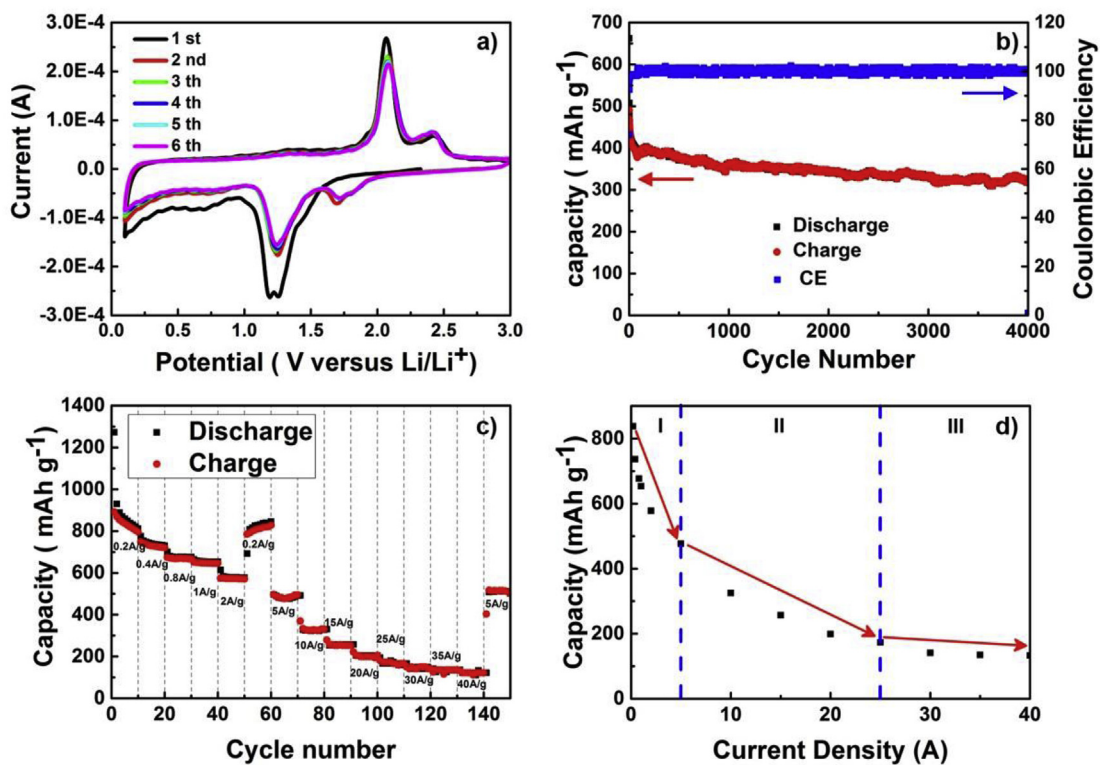


Fig. 4. (a) Representative CV curve of the NiCo<sub>2</sub>S<sub>4</sub>/Co<sub>9</sub>S<sub>8</sub>@G electrode for the first to sixth cycles at a scan rate of 0.1 mV s<sup>-1</sup>; (b) long term cycling performance of NiCo<sub>2</sub>S<sub>4</sub>/Co<sub>9</sub>S<sub>8</sub>@G electrode at a current density of 10 A g<sup>-1</sup>; (c) rate properties of the NiCo<sub>2</sub>S<sub>4</sub>/Co<sub>9</sub>S<sub>8</sub>@G electrode at current densities from 0.2 to 40 A g<sup>-1</sup>; (d) specific capacity vs. current densities plot of NiCo<sub>2</sub>S<sub>4</sub>/Co<sub>9</sub>S<sub>8</sub>@G electrode.

**Table 1**Comparison of the high-rate performance of this study with previously reported performance of Co<sub>9</sub>S<sub>8</sub> or NiCo<sub>2</sub>S<sub>4</sub>-based anode materials.

Anode (ref)	Discharge capacity	Current density	Cycle Number
Mesoporous Co <sub>9</sub> S <sub>8</sub> [23]	~150 mAh/g ~300 mAh/g	10 A/g 5 A/g	<100
Co <sub>9</sub> S <sub>8</sub> nanosheet on Ni foam [18]	~330 mAh/g	2 A/g	<100
MWCNT@a-C@Co <sub>9</sub> S <sub>8</sub> nanocomposite [19]	~500 mAh/g ~700 mAh/g	5 A/g 2 A/g	<100
MWCNT@Co <sub>9</sub> S <sub>8</sub> nanocomposite [19]	~400 mAh/g ~500 mAh/g	5 A/g 2 A/g	<100
MOF-derived hollow Co <sub>9</sub> S <sub>8</sub> @Graphite carbon nanocage [22]	~300 mAh/g ~250 mAh/g	5 C/g 10 C/g	<100
NiCo <sub>2</sub> S <sub>4</sub> nanosheet on Ni foam [12]	~900 mAh/g	2 A/g	<100
NiCo <sub>2</sub> S <sub>4</sub> nanosheet on Carbon cloth [15]	~600 mAh/g ~250 mAh/g	3.2 A/g 5 A/g	<100
<b>NiCo<sub>2</sub>S<sub>4</sub>/Co<sub>9</sub>S<sub>8</sub>@G</b> <i>this work</i>	<b>477 mAh/g</b> <b>323 mAh/g</b> <b>133 mAh/g</b>	<b>5 A/g</b> <b>10 A/g</b> <b>40 A/g</b>	<b>&lt;100</b> <b>4000</b> <b>&lt;100</b>

The bold style shows the results in our work.

with charge transfer at or near the surface of a redox active material; iii) non-Faradaic electrostatic interaction at the electrode/electrolyte interface (electrochemical double-layer capacitance EDLC) [27,32–36]. Charges can be electrochemically stored in either a Faradaic or a non-Faradaic manner depending on the kinetics of the redox charge-transfer reactions. It is demonstrated that if intercalation is kinetically facile enough to keep pace with a given charge/discharge rate, the fast and reversible intercalation of the system converges towards pseudocapacitance [36]. To check the storage mechanism involved in NiCo<sub>2</sub>S<sub>4</sub>/Co<sub>9</sub>S<sub>8</sub>@G electrode, the relation between specific capacity and current density is shown in Fig. 4d. The specific capacity is decreased with the increase of the current density from 0.2 to 40 A g<sup>-1</sup>. It is noteworthy that the trend of specific capacity vs current density has three stages: i) from 0.2 to 5 A g<sup>-1</sup>, the specific capacity decreases rapidly with the increase of current density, indicating slow discharge/charge kinetics involved in this stage. This process is mainly related to diffusion-controlled faradic reactions with slow solid-state ionic diffusion of 10<sup>-10</sup>–10<sup>-15</sup> cm<sup>2</sup> s<sup>-1</sup> into the bulk phase deeply; [37,38] ii) from 5 to 25 A g<sup>-1</sup>, the specific capacity decreases slowly with the increase of current density. The pseudocapacitive process is speculated to play an important role in this stage; iii) from 25 to 40 A g<sup>-1</sup>, the specific capacity remains relatively constant, and no longer changes with the current density. This specific capacity is mainly due to the non-Faradaic electrostatic interaction between Li<sup>+</sup> and Graphene or NiCo<sub>2</sub>S<sub>4</sub>/Co<sub>9</sub>S<sub>8</sub> nanocrystals. Obtained from Fig. 3d, it is speculated that a multi-faceted lithium storage mechanisms are involved in the NiCo<sub>2</sub>S<sub>4</sub>/Co<sub>9</sub>S<sub>8</sub>@G electrode. Moreover, the lithium storage kinetics might be governed by different mechanism with the change of current densities.

### 3.3. Lithium ion storage kinetics of NiCo<sub>2</sub>S<sub>4</sub>/Co<sub>9</sub>S<sub>8</sub>@G composites

In this section, we will examine the fundamental lithium storage properties of the NiCo<sub>2</sub>S<sub>4</sub>/Co<sub>9</sub>S<sub>8</sub>@G electrode. CVs collected between 0.1 and 6 mV s<sup>-1</sup> for NiCo<sub>2</sub>S<sub>4</sub>/Co<sub>9</sub>S<sub>8</sub>@G are shown in Fig. 5a and b. It can be observed that the current intensity increases along with the increase of scan rate. Under low scan rate ranged from 0.1–2 mV s<sup>-1</sup>, as shown in Fig. 5a, with the increase of scan rate, the position of reduction peak shifts to lower potential, while the position of oxidation peak shifts to higher potential. This shift phenomenon is attributed to sluggish lithium diffusion kinetics involved in conversion reaction. On the other hand, under high sweep rate ranged from 3–6 mV s<sup>-1</sup>, as shown in Fig. 5b, the peaks in the CVs show relatively little change in potential as a function of sweep rate, which is indicative of reversible reactions and fast

charge transfer processes. This implies rapid Li<sup>+</sup> insertion/deinsertion kinetics in our NiCo<sub>2</sub>S<sub>4</sub>/Co<sub>9</sub>S<sub>8</sub>@G electrode at high rate [39].

Galvanostatic discharge-charge (GDC) voltage profiles are also performed to complement the CV results, as shown in Fig. 5c and d. Under low current densities ranged from 0.2 to 2 A g<sup>-1</sup>, it is observed that the discharge plateaus of the NiCo<sub>2</sub>S<sub>4</sub>/Co<sub>9</sub>S<sub>8</sub>@G are clearly visible at these current densities. The discharge plateau is a certain distinct electrochemical feature to characterize conversion reaction which is a diffusion dominated charge storage process. In contrast to GDC under low current densities, at high current densities ranged from 5 to 15 A g<sup>-1</sup>, discharge plateaus vanish, and replaced by the pseudolinear galvanostatic traces, which clearly distinguish this charge storage mechanism from battery-type or diffusion dominated charge storage. The pseudolinear galvanostatic traces observed in GDC measurements, are expected for an extrinsically pseudocapacitive charge storage system, as demonstrated by Tolbert et al. and Mahmood et al. [28,39] The CV and GDC profiles give strong proof that the lithium storage of the NiCo<sub>2</sub>S<sub>4</sub>/Co<sub>9</sub>S<sub>8</sub>@G is governed by pseudocapacitive charge storage at high rate.

To further quantify the diffusion-controlled and capacitive charge storage processes (including both pseudocapacitive and EDLC contribution), the electrochemical lithium storage kinetics of NiCo<sub>2</sub>S<sub>4</sub>/Co<sub>9</sub>S<sub>8</sub>@G are investigated using the Trasatti analysis: [40–44]

$$q(v) = q_{\text{capacitive}} + a(v^{-1/2}) \quad (1)$$

$$\frac{1}{q(v)} = \frac{1}{q_{\text{tot}}} + a(v^{1/2}) \quad (2)$$

where  $q(v)$  is the total measured voltammetric charge transfer,  $q_{\text{capacitive}}$  refers to capacitive charge storage (both from double layer and pseudocapacitive processes),  $q_{\text{tot}}$  is the total amount of charge storage, and  $\alpha v^{-1/2}$  indicates charge storage associated with semi-infinite diffusion, where  $\alpha$  is a constant and  $v$  is the sweep rate. Utilizing Equation (1), as  $v \rightarrow \infty$ , access to the more diffusion-controlled redox sites are excluded and the intercept of the extrapolated capacity versus  $v^{-1/2}$  trend line gives the capacitive charge storage ( $q_{\text{capacitive}}$ ), which is calculated to be 407 mAh g<sup>-1</sup>, as shown in Fig. 5e. On the other hand, utilizing Equation (2), as  $v \rightarrow 0$ , the electrochemical reaction time-scale is long enough to allow access to all sites in the material and extrapolation of  $1/q(v)$  versus  $v^{1/2}$  gives the extrapolated total charge ( $q_{\text{tot}}$ ), which is calculated to be 988 mAh g<sup>-1</sup>, as shown in Fig. 5f. Combining the results obtained

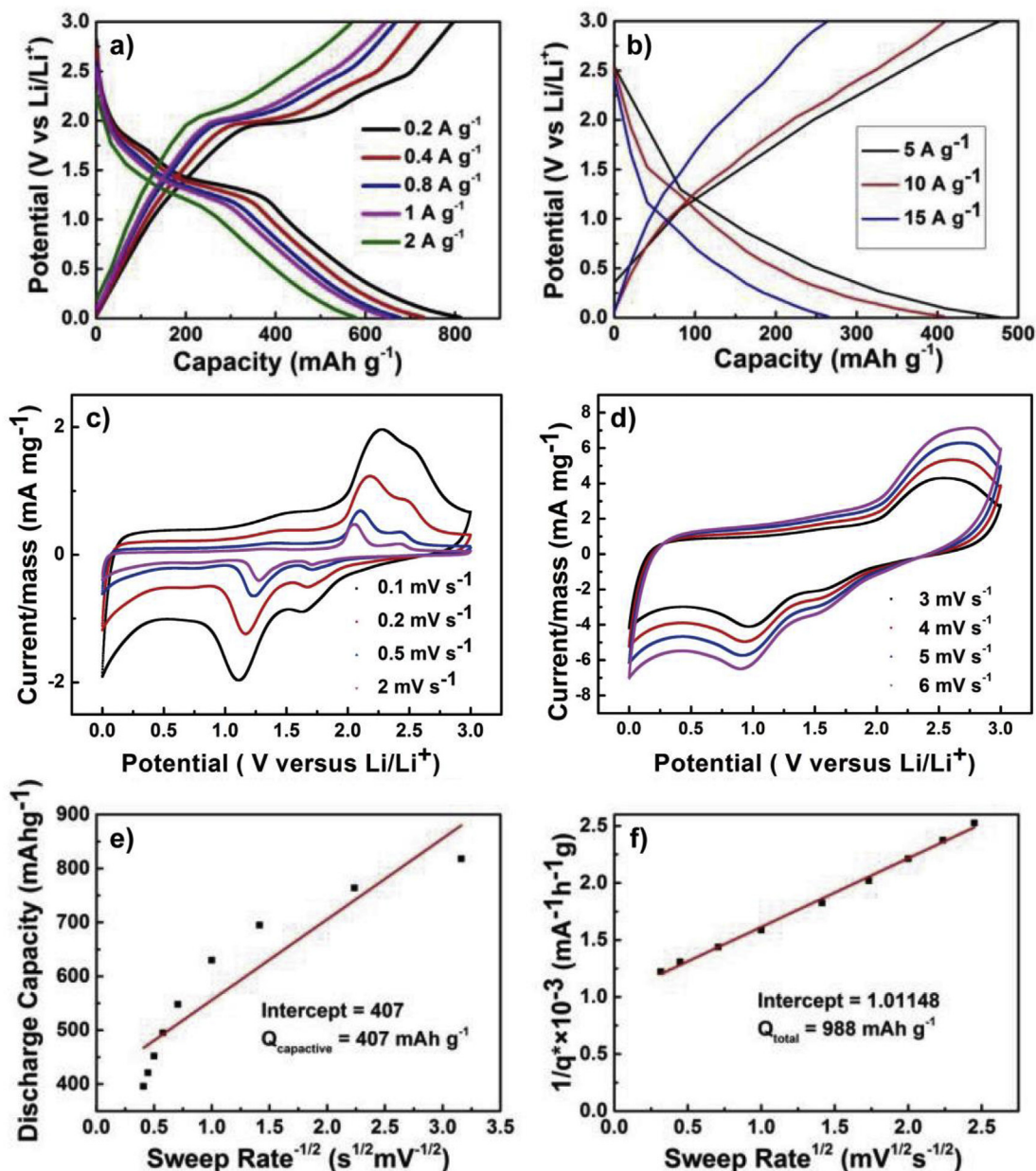


**Fig. 5.** (a) Galvanostatic charge-discharge voltage profiles of the NiCo<sub>2</sub>S<sub>4</sub>/Co<sub>9</sub>S<sub>8</sub>@G at a current density of 0.2–2 A g<sup>-1</sup>; (b) galvanostatic charge-discharge voltage profiles of the NiCo<sub>2</sub>S<sub>4</sub>/Co<sub>9</sub>S<sub>8</sub>@G at a current density of 5–15 A g<sup>-1</sup>; (c) CV curves of NiCo<sub>2</sub>S<sub>4</sub>/Co<sub>9</sub>S<sub>8</sub>@G electrode after 100 cycles at different sweep rates from 0.1 to 2 mV s<sup>-1</sup>; (d) CV curves of NiCo<sub>2</sub>S<sub>4</sub>/Co<sub>9</sub>S<sub>8</sub>@G electrode after 100 cycles at different sweep rates from 3 to 6 mV s<sup>-1</sup>. Trasatti analysis utilizing the dependence of voltammetric charge storage on the sweep rate. (e) As  $v \rightarrow \infty$  access to the more diffusion-controlled redox sites are excluded and extrapolation of capacity versus  $v^{-1/2}$  gives the capacitive charge storage ( $q_{\text{capacitive}}$ ), which is calculated to be 407 mAh g<sup>-1</sup>; (f) As  $v \rightarrow 0$  access to the diffusion limited redox sites can occur and so extrapolation of the inverse capacity versus  $v^{1/2}$  gives the extrapolated total charge ( $q_{\text{total}}$ , 988 mAh g<sup>-1</sup>).

from Fig. 5c and d, when the current density is extremely high (>25 A g<sup>-1</sup>), the specific density is due to the contribution of  $q_{\text{EDLC}}$  which is evaluated to be 140 mAh g<sup>-1</sup>. Using the relationship  $q_{\text{capacitive}} = q_{\text{pseudocapacitance}} + q_{\text{EDLC}}$ , we can conclude that  $q_{\text{pseudocapacitance}}$  is approximately 260 mAh g<sup>-1</sup>. Capacitive charge storage has the advantage of rendering high charging rate and therefore high power.

According to the above results, our rationally designed NiCo<sub>2</sub>S<sub>4</sub>/Co<sub>9</sub>S<sub>8</sub>@G electrode has following advantages for lithium ion storage: i) Graphene not only stabilize the formation of SEI, but also can function as the mechanical back bone and conductor medium [45,46]; ii) Co<sub>9</sub>S<sub>8</sub> phase ensures the robust cycle retention due to its

structural integrity [47]; iii) extremely fast kinetics is expected to be obtained by pseudo-capacitance in NiCo<sub>2</sub>S<sub>4</sub>/Co<sub>9</sub>S<sub>8</sub>@G. It has been proposed that the fast pseudocapacitance kinetic is due to the boosted metallic conductivity of NiCo<sub>2</sub>S<sub>4</sub>/Co<sub>9</sub>S<sub>8</sub>@G combined with an ideal nano-architecture with short ion diffusion path lengths and good electrolyte accessibility. This heterostructured nano-architecture is robust that can endure ultralong lithiation/delithiation cycling more than 4,000 cycles.

#### 4. Conclusions

In summary, we have successfully constructed hetero-NiCo<sub>2</sub>S<sub>4</sub>/

Co<sub>9</sub>S<sub>8</sub> nanocrystals anchored on Graphene (NiCo<sub>2</sub>S<sub>4</sub>/Co<sub>9</sub>S<sub>8</sub>@G) by an epitaxial growth mechanism. The synthesized NiCo<sub>2</sub>S<sub>4</sub>/Co<sub>9</sub>S<sub>8</sub>@G electrode exhibits 662 and 490 mAh g<sup>-1</sup> capacity at the first discharge/charge cycle and can be maintained at 323 mAh g<sup>-1</sup> after 4000 cycles (from 2nd cycle only 0.008% decay per cycle) at an ultrahigh current density of 10 A g<sup>-1</sup>. Moreover, NiCo<sub>2</sub>S<sub>4</sub>/Co<sub>9</sub>S<sub>8</sub>@G electrode can be full charged/discharge within 11 s while still achieving a specific capacity of 133 mAh g<sup>-1</sup> at a current density of 40 A g<sup>-1</sup>. These results not only confirm the superior lithium storage properties of the NiCo<sub>2</sub>S<sub>4</sub>/Co<sub>9</sub>S<sub>8</sub>@G, but also cast new light on the development of high-rate performance anode materials for sodium ion batteries and supercapacitors.

## Acknowledgments

This work was financially supported by the National Natural Science Foundation of China (Nos. 51372040, 51701042, 51601040), the Shanghai Rising-Star Program (16QA1400700).

## Appendix A. Supplementary data

Supplementary data related to this article can be found at <https://doi.org/10.1016/j.jallcom.2018.02.340>.

## References

- [1] R.V. Noorger, Nature 507 (2014) 26–28.
- [2] M. Armand, J.M. Tarascon, Nature 451 (2008) 652–657.
- [3] J.M. Tarascon, M. Armand, Nature 414 (2001) 359–367.
- [4] B. Dunn, H. Kamath, J.M. Tarascon, Science 334 (2011) 928–935.
- [5] Y. Fu, Z. Zhang, X. Yang, Y. Gan, W. Chen, RSC Adv. 5 (2015) 86941–86944.
- [6] J. Yu, S.M. Chen, W.J. Hao, S.J. Zhang, ACS Nano 10 (2016) 2500–2508.
- [7] B.S. Lee, J. Yoon, C. Jung, D.Y. Kim, S.Y. Jeon, K.H. Kim, J.H. Park, H. Park, K.H. Lee, Y.S. Kang, J.H. Park, H. Jung, W.R. Yu, S.G. Doo, ACS Nano 10 (2016) 2617–2627.
- [8] S. Wu, R. Xu, M. Lu, R. Ge, J. Iocozzia, C. Han, B. Jiang, Z. Lin, Adv. Energy Mater. 5 (2015) 1500400.
- [9] Y. Zheng, T.F. Zhou, C.F. Zhang, J.F. Mao, H.K. Liu, Z.P. Guo, Angew. Chem. Int. Ed. 55 (2016) 3408–3413.
- [10] S. Goriparti, E. Miele, F.D. Angelis, E.D. Fabrizio, R.P. Zaccaria, C. Capiglia, J. Power Sources 257 (2014) 421–443.
- [11] Y. Zhao, X. Li, B. Yan, D. Xiong, D. Li, D. Lawes, X.L. Sun, Adv. Energy Mater. 6 (2016) 1502175.
- [12] J.G. Wang, D. Jin, R. Zhou, C. Shen, K. Xie, B. Wei, J. Power Sources 306 (2016) 100–106.
- [13] C. Xia, P. Li, A.N. Gandhi, U. Schwingenschlögl, H.N. Alshareef, Chem. Mater. 27 (2015) 6482–6485.
- [14] W. Yang, L. Chen, J. Yang, X. Zhang, C. Fang, Z. Chen, L. Huang, J. Liu, Y. Zhou, Z. Zou, Chem. Commun. J. Chem. Soc. Sect. D 52 (2016) 5258–5261.
- [15] R. Zou, Z. Zhang, M.F. Yuen, M. Sun, J. Hu, C.S. Lee, W. Zhang, NPG Asia Mater. 7 (2015) 195.
- [16] X. Wu, S. Li, B. Wang, J. Liu, M. Yu, Phys. Chem. Chem. Phys. 18 (2016) 4505–4512.
- [17] Y. Song, Z. Chen, Y. Li, Q. Wang, F. Fang, Y.N. Zhou, L. Hu, D. Sun, J. Mater. Chem. 5 (2017) 9022–9031.
- [18] R. Jin, J. Zhou, G. Li, L. Yang, Mater. Lett. 163 (2016) 183–186.
- [19] Y. Zhou, D. Yan, H. Xu, S. Liu, J. Yang, Y. Qian, Nanoscale 7 (2015) 3520–3525.
- [20] H. Wang, S. Lu, Y. Chen, L. Han, J. Zhou, X. Wu, W. Qin, J. Mater. Chem. 3 (2015) 23677–23683.
- [21] J. Mujtaba, H. Sun, G. Huang, Y. Zhao, H. Arandiyani, G. Sun, S. Xu, J. Zhu, RSC Adv. 6 (2016) 31775–31781.
- [22] J. Liu, C. Wu, D. Xiao, P. Kopold, L. Gu, P.A.V. Aken, J. Maeir, Y. Yan, Small 17 (2016) 2354–2364.
- [23] Y. Zhou, D. Yan, H. Xu, J. Feng, X. Jiang, J. Yue, J. Yang, Y. Qian, Nano Energy 12 (2015) 528–537.
- [24] L.R. Hou, Y.Y. Shi, S.Q. Zhu, R.H. Muhammad, G. Pang, X.G. Zhang, C.Z. Yuan, J. Mater. Chem. 5 (2017) 133–144.
- [25] X. Hong, J. Kim, S. Shi, Y. Zhang, C. Jin, Y. Sun, S. Tongay, J. Wu, Y. Zhang, F. Wang, Nat. Nanotechnol. 9 (2014) 682–686.
- [26] J. Nishitani, K. Yu, W. Walukiewicz, Appl. Phys. Lett. 105 (2014) 103–132.
- [27] D. Chao, C. Zhu, P. Yang, X. Xia, J. Liu, J. Wang, X. Fan, S.V. Savilov, J. Lin, Z.X. Shen, Nat. Commun. 7 (2016) 12122.
- [28] D. Mahmood, S.K. Park, K.D. Kwon, S.J. Chang, J.Y. Hong, G.Z. Shen, Y.M. Jung, T.J. Park, S.W. Khang, W.S. Kim, J. Kong, H.S. Park, Adv. Energy Mater. 6 (2016) 1501115.
- [29] Y. Song, Y. Cao, J. Wang, Y.N. Zhou, F. Fang, Y. Li, S.P. Gao, Q.F. Gu, L. Hu, D. Sun, ACS Appl. Mater. Interfaces 8 (2016) 21334–21342.
- [30] W. Qin, L. Han, H. Bi, J. Jian, X. Wu, P. Gao, Nanoscale 7 (2015) 20180–20187.
- [31] A.S. Sarac, Microelectron. Eng. 83 (2006) 1534–1537.
- [32] W.L. Qian, S. Krimm, Biopolymers 32 (1992) 1503–1518.
- [33] F. Zou, X. Hu, L. Qie, Y. Jiang, X. Xiong, Y. Qiao, Y. Huang, Nanoscale 6 (2014) 924–930.
- [34] R. Wang, S. Wu, Y. Lv, Z. Lin, Langmuir 30 (2014) 8215–8220.
- [35] V. Augustyn, P. Simon, B. Dunn, Energy Environ. Sci. 7 (2014) 1597–1614.
- [36] S. Li, J. Qiu, C. Lai, M. Ling, H. Zhao, S. Zhang, Nanomater. Energy 12 (2015) 224–230.
- [37] P. Yu, C. Li, X. Guo, J. Phys. Chem. C 118 (2014) 10616–10624.
- [38] V. Augustyn, J. Come, M.A. Lowe, J.W. Kim, P.L. Taberna, S.H. Tolbert, H.D. Abruna, P. Simon, B. Dunn, Nat. Mater. 12 (2013) 518–522.
- [39] M. Park, X. Zhang, M. Chung, G.B. Less, A.M. Sastry, J. Power Sources 195 (2010) 7904–7929.
- [40] N. Balke, S. Jesse, A.N. Morozovska, E. Eliseev, D.W. Chung, Y. Kim, L. Adamczyk, R.E. Garcia, N. Dudney, S.V. Kalinin, Nat. Nanotechnol. 5 (2010) 749–754.
- [41] S. Ardizzzone, G. Fregonara, S. Trasatti, Electrochem. Acta 35 (1990) 263–267.
- [42] K.M. Lin, K.H. Chang, C.C. Hu, Y.Y. Li, Electrochem. Acta 54 (2009) 4574–4581.
- [43] C. Jo, I. Hwang, J. Lee, C.W. Lee, S. Yoon, J. Phys. Chem. C 115 (2011) 11880–11886.
- [44] X. Wang, L. Fan, D. Gong, J. Zhu, Q. Zhang, B. Lu, Adv. Funct. Mater. 26 (2016) 1104–1111.
- [45] S.Y. Zheng, F. Fang, G.Y. Zhou, G.R. Chen, L.Z. Ouyang, M. Zhu, D.L. Sun, Chem. Mater. 20 (2008) 3954–3958.
- [46] Y. Song, Y.M. Li, L. Zhu, Z.C. Pan, Y.C. Jiang, P. Wang, Y.N. Zhou, F. Fang, L.F. Hu, D.L. Sun, J. Mater. Chem. 6 (2018) 1086–1093.
- [47] Z.L. Chen, R.B. Wu, M. Liu, H. Wang, H.B. Xu, Y.H. Guo, Y. Song, F. Fang, X.B. Yu, D.L. Sun, Adv. Funct. Mater. 27 (2017) 1702046.